

# Harnessing exciton-exciton annihilation in two-dimensional semiconductors

Eric Linaryd,<sup>1,2</sup> Dinesh Yadav,<sup>3,4</sup> Daniele Vella,<sup>1,2</sup> Ivan A. Verzhbitskiy,<sup>1,2</sup>

Kenji Watanabe,<sup>5</sup> Takashi Taniguchi,<sup>5</sup> Fabian Pauly,<sup>3,4</sup> Maxim Trushin,<sup>2\*</sup> and Goki Eda<sup>1,2,6\*</sup>

<sup>1</sup>*Department of Physics, National University of Singapore, Singapore*

<sup>2</sup>*Centre for Advanced 2D Materials, National University of Singapore, Singapore*

<sup>3</sup>*Okinawa Institute of Science and Technology Graduate University, Onna-son, Okinawa 904-0495, Japan*

<sup>4</sup>*Department of Physics, University of Konstanz, 78457 Konstanz, Germany*

<sup>5</sup>*National Institute for Material Science, 1-1 Namiki, Tsukuba 305-0044, Japan and*

<sup>6</sup>*Department of Chemistry, National University of Singapore, Singapore*

(Dated: April 21, 2020)

Strong many-body interactions in two-dimensional (2D) semiconductors give rise to efficient exciton–exciton annihilation (EEA). This process is expected to result in the generation of unbound high energy carriers. Here, we report an unconventional photoresponse of van der Waals heterostructure devices resulting from efficient EEA. Our heterostructures, which consist of monolayer transition metal dichalcogenide (TMD), hexagonal boron nitride (hBN), and few-layer graphene, exhibit photocurrent when photoexcited carriers possess sufficient energy to overcome the high energy barrier of hBN. Interestingly, we find that the device exhibits moderate photocurrent quantum efficiency even when the semiconducting TMD layer is excited at its ground exciton resonance despite the high exciton binding energy and large transport barrier. Using *ab initio* calculations, we show that EEA yields highly energetic electrons and holes with unevenly distributed energies depending on the scattering condition. Our findings highlight the dominant role of EEA in determining the photoresponse of 2D semiconductor optoelectronic devices.

Keywords: 2D materials, transition metal dichalcogenides, van der Waals heterostructures, exciton–exciton annihilation, optoelectronic devices

Many-body effects manifest themselves as unique photoresponse in nanoscale materials [1]. Exciton–exciton annihilation (EEA), a four-body interaction involving the energy and momentum transfer between two holes and two electrons, is known to be highly efficient in nanostructures with reduced dimensions, such as quantum dots [2, 3], graphene nanoribbons [4], carbon nanotubes [5, 6], and polymer chains [7, 8]. Recent studies [9–11] indicate that the EEA rate in two-dimensional (2D) Group VI transition metal dichalcogenide (TMD) semiconductors is substantially enhanced even when compared to their bilayer and trilayer samples [12]. While the EEA in 2D semiconductors leads to undesirable efficiency droop in photoluminescence (PL) [13] and electroluminescence (EL) [14], energy conservation requires hot electron-hole pairs to be generated upon annihilation of individual excitons. Recent study showed that the EEA-generated hot carriers can be harnessed for remarkably efficient optical upconversion in 2D TMD semiconductors [15, 16], and their heterostructures [17], inspiring prospects for harnessing highly efficient EEA process in 2D materials to generate hot carriers for energy harvesting application.

Herein, we report photoresponse originating from EEA-generated hot carriers in a metal-insulator-semiconductor (MIS)-type van der Waals heterostructure device. In this study, “hot” carrier refers to non-

thermalized high energy carriers generated by EEA in contrast to thermalized hot carriers in graphene-based photothermoelectric devices [18–20]. The MIS-type heterostructure consists of few-layer graphene (FLG), hexagonal boron nitride (hBN), and monolayer molybdenum disulfide (MoS<sub>2</sub>) (Figure 1a). The bright optical microscope and atomic force microscope (AFM) image of one of the MIS devices is displayed in the Supporting Information Figure S1. Figure 1b depicts the schematic band diagram of the heterostructure. Because of the low electron affinity and wide band gap of hBN (Figure 1b), it acts as an insulating barrier which blocks charge transfer between the FLG and the MoS<sub>2</sub> layer. However, the band alignment between hBN with FLG and MoS<sub>2</sub> reveals significantly lower energy barrier for interlayer hole transfer compared to electron transfer [21–25]. Hence, hBN acts as a carrier- and energy-selective tunnel barrier that selectively favors hot hole transfer. Under forward bias above a specific threshold voltage ( $V_d > V_{th}$ ), the device exhibits EL at low threshold current densities, evidencing hole tunneling from FLG to MoS<sub>2</sub>. The tunnel barrier for holes in reverse bias ( $V_d < 0$ ) is similarly low, however, the device remains highly insulating due to the absence of holes in MoS<sub>2</sub>. The charge transport and EL behavior of the tunnel diode are discussed in Supporting Information S3 and in a previous study [14].

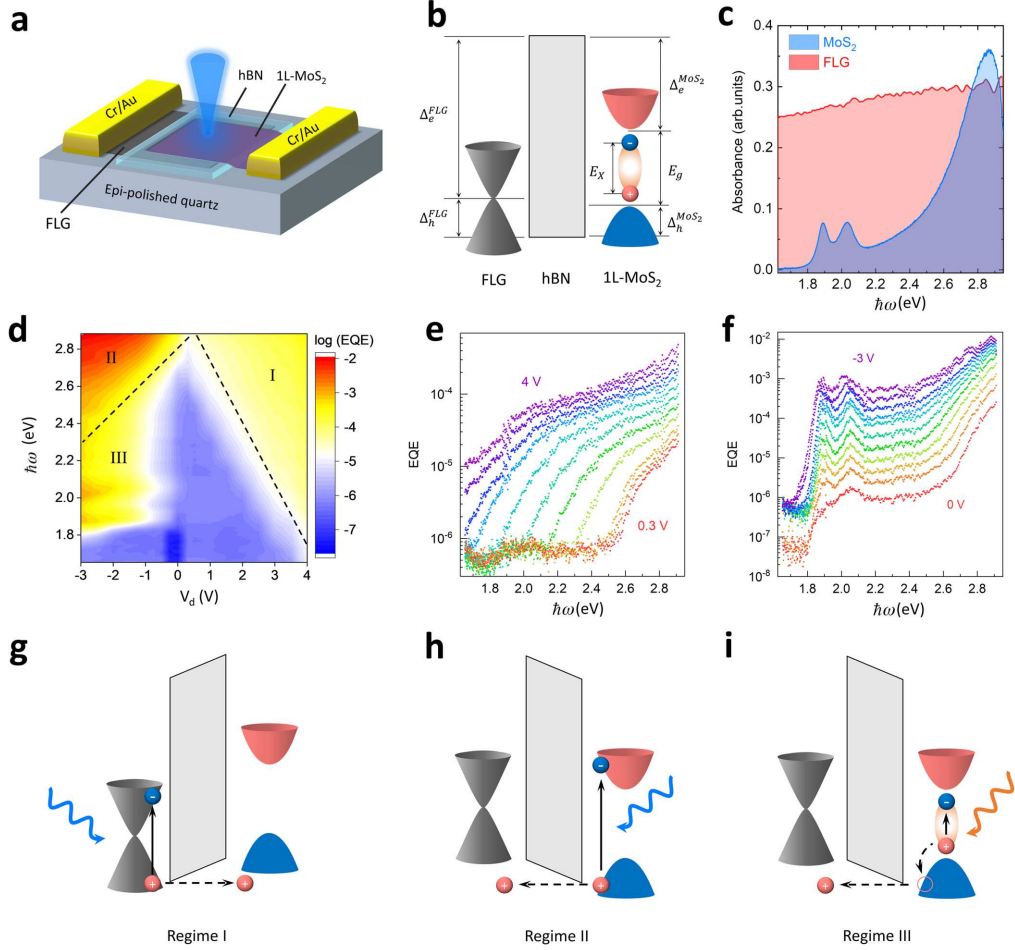


FIG. 1: Photocurrent response of FLG/hBN/MoS<sub>2</sub> heterostructure device. **a**, Schematic of a FLG/hBN/MoS<sub>2</sub> heterostructure irradiated by a laser beam. **b**, Schematic band diagram in flat band condition.  $E_X$  and  $E_g$  represent excitonic and quasiparticle band gap of monolayer MoS<sub>2</sub>.  $\Delta_h^{FLG}$ ,  $\Delta_h^{MoS_2}$ ,  $\Delta_e^{FLG}$ , and  $\Delta_e^{MoS_2}$  represent the energy barrier for interlayer hole and electron transport at FLG/hBN and hBN/MoS<sub>2</sub> interfaces, respectively. **c**, Absorbance spectrum of FLG and monolayer MoS<sub>2</sub>. **d**, Color plot of EQE measured as a function of the excitation photon energy and bias voltage. The blue region corresponds to low EQE below the detection limit. The origin of finite EQE in the yellow and red regions I, II, and III is explained in panels **g**, **h**, and **i**, respectively. Dashed lines are guides to the eye, separating the regimes I, II, and III. **e**, EQE measured as a function of the excitation energy at different forward biases (0.3, 0.4, 0.5, 1, 1.5, 2, 2.5, 3, 3.5, 3.75, 4 V). **f**, EQE measured as a function of the excitation energy at different reverse biases (0, -0.25, -0.5, -0.75, -1, -1.25, -1.5, -1.75, -2, -2.5, -3 V). (**g**-**i**), Schematic describing the photocurrent generation mechanism. In **g**, hole is photoexcited in FLG and transferred to MoS<sub>2</sub> across the hBN barrier in forward bias. In **h**, photoexcited high energy non-thermalized hole is emitted from MoS<sub>2</sub> to FLG in reverse bias. **i**, Hot hole is created following formation of ground exciton in MoS<sub>2</sub> and transferred to FLG. Here, the excitation energy is below the quasiparticle band gap of MoS<sub>2</sub> and the heterostructure is under reverse bias.

We investigate the photocarrier dynamics of the heterostructure by measuring the bias-dependent spectral features in the photocurrent generated by photons of varying energy ranging from 1.65 to 2.91 eV. All photocurrent measurements were performed with lock-in technique (Supporting Information S1) [26] at room temperature and in vacuum ( $10^{-5}$  mbar). On the basis of the band alignment of the heterostructure, non-negligible photocurrent is only expected when the photoexcited carriers gain sufficient energy to overcome the potential barrier due to hBN (Figure 1b). Note that the FLG exhibits

relatively uniform absorption across the visible frequencies whereas monolayer MoS<sub>2</sub> absorption exhibits prominent excitonic resonances with three excitonic peaks (Figure 1c). Two types of excitons, A and B, at 1.89 eV and 2.03 eV arise from spin-orbit split bands. Figure 1d shows the external quantum efficiency (EQE), the incident photon to converted electron ratio, as a function of the excitation energy  $\hbar\omega$  and bias  $V_d$ . The EQE value is calculated from the measured photocurrent ( $I_{PC}$ ) as  $EQE = (I_{PC}/P) \cdot (\hbar\omega/e)$ , where  $P$  is the optical power, and  $e$  is the elementary charge.

The spectral features are distinctly different in the forward (Figure 1e) and reverse (Figure 1f) bias regimes, but the common trend is the presence of distinct threshold behaviour. In forward bias, the photocurrent remains negligible at low photon energy before increasing exponentially above the threshold photon energy  $\hbar\omega_{\text{th}}$ . The  $\hbar\omega_{\text{th}}$ , in turn, decreases linearly with increasing  $V_d$ , as shown by the dashed line in Figure 1d. The photocurrent spectrum is featureless above the threshold with no traces of excitonic absorption, suggesting that photocarriers generated in FLG play a dominant role in photocurrent generation (regime I). The maximum  $\hbar\omega_{\text{th}}$  is  $\sim 2.6$  eV at low bias. Here,  $\hbar\omega_{\text{th}}/2$  coincides with the difference between the neutrality point of FLG and the valence-band maximum of hBN, corresponding to the energy barrier for interlayer hole transfer from FLG to MoS<sub>2</sub> based on previous studies on photocarrier transport across graphene/hBN interface [22, 23] (Figure 1b). This indicates that the interlayer charge transport of non-thermalized photo-carriers, possibly by Fowler–Nordheim tunnelling or over-barrier direct transport, is responsible for the observed photocurrent above  $\hbar\omega_{\text{th}}$  (Figure 1g). Under reverse bias, EQE exhibits a similar threshold behaviour but with two prominent peaks corresponding to A and B excitonic absorption resonances. At the first sight, the threshold behavior can be explained as the onset of hot hole direct tunneling from MoS<sub>2</sub> to FLG (see Figure 1h, regime II), similar to the forward bias case albeit in opposite direction. On the other hand, the relatively strong photocurrent in the low-energy excitation regime is unexpected due to high binding energy of excitons and their insufficient kinetic energy to overcome the potential barrier of hBN. Remarkably, the EQE at the exciton resonance in this regime III is comparable to those in regime II, specially under strong reverse bias. The observation of a finite photocurrent at the excitation energy below the quasiparticle bandgap of MoS<sub>2</sub> indicates exciton dissociation generating hot holes with sufficient excess energy to overcome potential barrier due to hBN (see Figure 1i).

There are two possible mechanisms for hot holes generation through exciton dissociation: disorder-assisted exciton decay and EEA [27]. The exciton dissociation rate through the first mechanism varies linearly with exciton density [28] while the latter varies quadratically [29]. To distinguish these two mechanisms, we measured photoluminescence (PL) and the photocurrent as a function of excitation power at the excitation energy near the ground-state exciton resonance, well below the quasiparticle band gap of MoS<sub>2</sub> and energy required for hole tunnelling from monolayer MoS<sub>2</sub> to FLG (Figure 1d,f). This allows us to determine whether the same rate constants consistently describe the behavior of these interdependent phenomena. Figure 2a shows the power dependence of the PL quantum yield (QY) and photocurrent internal quantum efficiency (IQE) measured concurrently on the

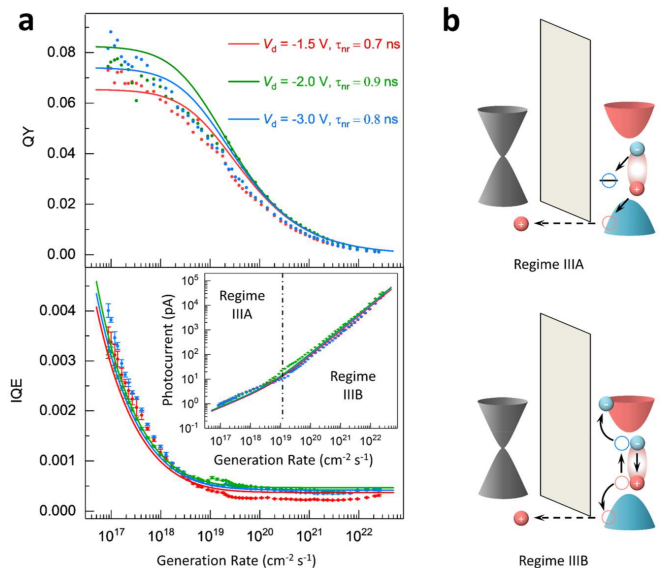


FIG. 2: Photocurrent and PL measurement of exciton–exciton annihilation in monolayer MoS<sub>2</sub>. **a**, QY and IQE measured under the same experimental conditions and consistently fitted as functions of  $g_{\text{eh}}$  using different values of  $\tau_{\text{nr}}$  for each  $V_d$ . The experimental data is taken at voltages lower than  $-1$  V to reduce electron doping and to obtain higher QY [30]. QY is deduced from equation (1) with  $k_{\text{XX}} = 0.1$  cm<sup>2</sup>/s and  $\tau_r = 10$  ns. IQE is derived from equation (2) assuming  $\tau_{\text{tr}} = 3.75$  ns and  $k_{\text{CC}} = 5 \times 10^4$  cm<sup>2</sup>/s. The inset shows the photocurrent measured and calculated from equation (2). The trend changes at a generation rate of about  $10^{19}$  cm<sup>-2</sup>s<sup>-1</sup>, indicating activation of EEA processes. The excitation energy is about 1.96 eV. **b**, Schematics describing photocurrent generation mechanisms. The upper panel shows a charge-trapping process generating a high-energy free hole corresponding to regime IIIA in **a**. The lower panel describes an EEA process generating a pair of hot carriers, corresponding to regime IIIB in **b**.

same sample with 633 nm (1.96 eV) laser as the excitation source. The experimental details and the calculation of PL QY and IQE are described in Supporting Information S1.

The PL QY is nearly constant at low photocarrier generation rates and gradually decreases with increasing radiation power. In contrast, the photocurrent IQE drops initially and saturates to a finite value in the high-power regime. The steady-state exciton concentration  $n_X$  can be found by balancing the electron-hole generation rate  $g_{\text{eh}}$  with the total exciton decay rate as

$$k_{\text{XX}}n_X^2 + \frac{n_X}{\tau_X} = g_{\text{eh}}, \quad (1)$$

where  $k_{\text{XX}}$  is the EEA rate,  $\tau_X^{-1} = \tau_r^{-1} + \tau_{\text{nr}}^{-1}$  is the reciprocal exciton lifetime with  $\tau_r$  and  $\tau_{\text{nr}}$  being the radiative and non-radiative exciton relaxation times, respectively. The latter is mostly due to charge traps [28]

with an additional contribution from electron-exciton annihilation [30], which is particularly relevant for n-doped samples. The charge traps are expected to be sulfur vacancies, which are the most energetically favorable type of defect [31]. By tuning the Fermi level through an external electric field, we change the equilibrium occupation of traps altering their charge trapping efficiency. Thus, the electron-exciton annihilation rate also changes with bias [30]. Hence,  $\tau_{nr}$  differs for each PL QY curve shown in Figure 2a. The theoretical QY is given by the ratio between radiative recombination and generation rates,  $QY = n_X/(\tau_r g_{eh})$ , where  $n_X$  is the solution of equation (1). In the low-power (or linear-response) limit, the QY approaches a constant given by the ratio  $\tau_X/\tau_r$  that at the same time determines the maximum QY for a given voltage. In the high-power limit the QY decreases with increasing  $g_{eh}$  as  $QY \sim 1/(\tau_r \sqrt{g_{eh} k_{XX}})$  because EEA reduces the steady-state concentration of excitons. The kinetic model in equation 1 describes the power-dependence of QY observed in experimental data with fitting parameters of  $k_{XX} = 0.1 \text{ cm}^2/\text{s}$ ,  $\tau_r = 10 \text{ ns}$  and  $\tau_{nr} = 0.7 \text{ to } 0.9 \text{ ns}$ . The fitting parameters are consistent with earlier studies in monolayer MoS<sub>2</sub> [9, 29] and other 2D semiconductors such as MoSe<sub>2</sub>[11], WS<sub>2</sub> [12], and WSe<sub>2</sub>[10].

While EEA leads to reduction of exciton population and therefore diminishes the PL QY, it generates hot carriers that can overcome the hBN barrier and contribute to photocurrent. For the IQE model, we consider the concentration of such hot holes denoted by  $N$ . Here, EEA competes with high-energy carrier-carrier collisions leading in particular to impact ionization, which is described by the rate  $k_{CC}$  of the order of  $10^4 \text{ cm}^2/\text{s}$ . The same process makes the high-energy holes thermalize by collisions with lower energy carriers, hence, lose the energy required to escape the semiconductor. At the typical  $N \sim 10^9 - 10^{10} \text{ cm}^{-2}$ , the corresponding carrier-carrier collision time is of the order of  $10 - 100 \text{ fs}$ , consistent with literature values in bulk [32] and 2D semiconductors [33, 34]. The rate equation for  $N$  can be written as

$$k_{XX} (g_{eh} \tau_X)^2 + \frac{g_{eh} \tau_X}{\tau_{nr}} = k_{CC} N^2 + \frac{N}{\tau_{tr}}, \quad (2)$$

where  $\tau_{tr}$  is the interlayer transport time (ns scaled), and the corresponding  $IQE = N/(\tau_{tr} g_{eh})$  is given by the ratio between the transport and generation rates. Equation (2) is deduced in Supporting Information S1. In contrast to a recent work [35], we do not use ultrafast pulses and consider the rate equation in the steady-state limit. The model does not account for the carrier-phonon interactions because photocarrier thermalization is dominated by the carrier-carrier scattering away from the band edges [36].

The defect-assisted non-radiative recombination is also responsible for the hole generation (as shown in Figure

2b) that connects equations (1) and (2). In the simplest case, when no barrier exists and all the photoexcited carriers can escape the semiconductor, the terms containing  $k_{XX}$  and  $k_{CC}$  are not relevant, and we obtain  $IQE = \tau_X/\tau_{nr}$ . In MIS heterostructure case, the hBN barrier places the hole escape window to rather high energies ( $\sim 0.4 \text{ eV}$  or greater with respect to the top of the MoS<sub>2</sub> valence band), and the holes rapidly leave the window while thermalizing. Because of carrier-carrier scattering being a quadratic function of carrier concentration, the resulting IQE is strongly diminished with increasing excitation rate. However, EEA compensates the carrier-thermalization process at high excitation densities and prevents the IQE from falling to zero. In the limit of high photocarrier generation rates, we obtain a saturated IQE independent of  $g_{eh}$  given by

$$IQE_{\text{sat}} = \frac{\tau_X}{\tau_{tr}} \sqrt{\frac{k_{XX}}{k_{CC}}}, \quad k_{XX} g_{eh} \tau_X \tau_{tr} \gg 1. \quad (3)$$

This model fits the experimentally observed trend, as shown in Figure 2a. The saturation of the IQE at high photocarrier generation rates is a clear manifestation that the photocurrent generation involves EEA.

In EEA process, nonradiative exciton recombination ionizes another exciton. Considering energy conservation law, the ionization energy is equal to the energy released during recombination process. This recombination energy is equal to excitation energy  $E_X^A$  and  $E_X^B$  for excitons A and B, respectively. Ionization energy equals the sum of the exciton binding energy and the excess energy shared between the free electron and hole created. The exciton binding energies are given as follows:  $E_b^{A,B} = E_g - E_X^{A,B}$ . Further, the momentum conservation law dictates that the electron and hole wave vectors of ionized exciton must be opposite in direction, although equal in magnitude, in the absence of Umklapp processes. Hence, there is a finite range of possible allowed states in electronic structure of MoS<sub>2</sub> that satisfies the energy and momentum restrictions. Here, we identify the allowed transition states within the first Brillouin zone of MoS<sub>2</sub> EEA processes to generate hot carriers that can contribute to photocurrent generation using density functional theory (DFT) modeling. The wave vectors are counted with respect to the corner of the Brillouin zone, where the electron-hole pairs emerge due to EEA. Through scissor operators, we manually adjust the quasiparticle bandgap to the experimental value of  $E_g = 2.24 \text{ eV}$  since the theory does not reliably predict quasiparticle energies [37]. Figure 3a,b shows the band structure, density of states (DOS), and the DOS weighted with the probability to occupy the states due to EEA. Figure 3c,d shows the final wave vectors of electrons and holes in the Brillouin zone with their excess energies encoded in color. Note that the final electron and hole states are asymmetric such that one of the two resulting particles tends to gain more energy than the other. To contribute

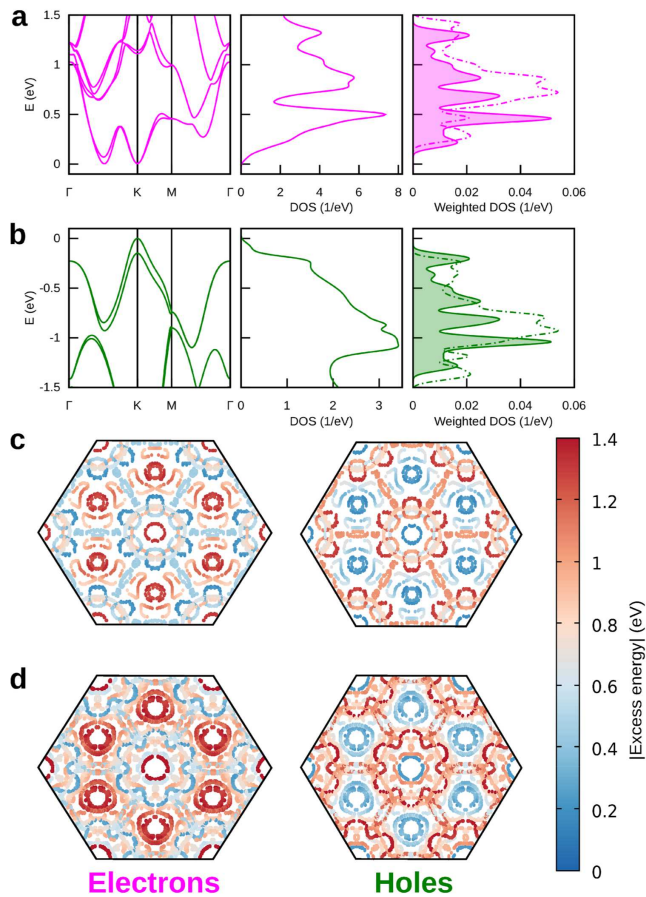


FIG. 3: Energy of EEA-derived carriers in MoS<sub>2</sub>. **a**, Conduction band structure (left), conduction band DOS (center), and the DOS weighted by the EEA probability for the type-A (filled solid curve) and type-B (dot-dashed curve) excitons (right). **b**, Same as **a** for valence bands. **c**, The Brillouin-zone regions accessible to the electrons (left) and holes (right), derived for the type-A exciton EEA. The regions are color-coded with the electron and hole excess energies counted from the valence- and conduction-band edges, respectively. **d**, Similar to **c** for the type-B excitons.

to photocurrent generation, hot free holes need to overcome the transport barrier due to hBN band gap. The excess energy required is estimated to be 0.4 eV or greater (Figure 1b) [21]. Our DFT modeling demonstrates that holes derived from recombination of both A and B excitons possess sufficient excess kinetic energies ( $> 1$  eV) to contribute to photocurrent (Figure 2b).

In summary, we have shown that EEA in 2D semiconductors can be harnessed in photocarrier transport in vdW heterostructures. EEA rate in 2D semiconductor is significantly enhanced compared to bulk semiconductor to generate clear photoresponse in the excitation power range of ordinary optoelectronic devices, corresponding to photocarrier generation rates greater than  $10^{19}$  cm<sup>-2</sup>s<sup>-1</sup>. We note that the observed effect is not

limited to monolayer MoS<sub>2</sub>. We have also observed the equivalent effects in devices based on FLG/hBN/WS<sub>2</sub> heterostructure despite higher barrier that the holes must overcome to yield photocurrent (see Supporting Information S5). Although the efficiency of these unoptimized devices is limited, we envision that an intelligent heterostructure design by material selection and band gap engineering will enable improved energy-harvesting devices by exploiting EEA processes in 2D semiconductors.

## Contributions

G.E. and E.L. conceived the idea of the work. E.L. fabricated the MIS heterostructure devices and performed electro-optical measurements and other sample characterizations with guidance from I.V. and D.V. I.V. and D.V. devised and assembled the necessary electro-optical setup. D.Y. theoretically explored the EEA generation channels under supervision of F.P. and M.T. K.W. and T.T. provided hBN crystals. M.T. and G.E. managed the project, analyzed the data, devised the model, and wrote the manuscript with inputs from E.L., D.Y. and F.P.

## Acknowledgements

G.E. acknowledge the Singapore National Research Foundation (NRF) for funding the research under the Medium Sized Centre Programme R-723-000-001-281. G.E. also acknowledges support from the Ministry of Education (MOE), Singapore, under AcRF Tier 2 (MOE2017T2-1-134) and Tier 3 (MOE2018-T3-1-005). K.W. and T.T. acknowledge support from the Elemental Strategy Initiative conducted by the MEXT, Japan and the CREST (JPMJCR15F3), JST. M.T. acknowledges the Director's Senior Research Fellowship from the Centre for Advanced 2D Materials at the National University of Singapore (funded jointly through Singapore NRF Medium Sized Centre Programme [R-723-000-001-281] and NUS Young Investigator Award [R-607-000-236-133]). D.Y. and F.P. were funded by the Collaborative Research Center (SFB) 767 of the German Research Foundation (DFG). An important part of the numerical modeling was carried out on the computational resources of the bwHPC program, namely the bwUniCluster and the JUSTUS HPC facility.

## Competing Interests

The authors declare no competing interests.

## Additional Information

Supporting Information is available free of charge at <https://pubs.acs.org/doi/10.1021/acs.nanolett.9b04756>

Correspondence and requests for supplemental materials should be addressed to either M.T. (theory, [c2dmt@nus.edu.sg](mailto:c2dmt@nus.edu.sg)) or G.E. (experiment, [g.eda@nus.edu.sg](mailto:g.eda@nus.edu.sg)).

- 
- [1] K. F. Mak and J. Shan, *Nature Photonics* **10**, 216 (2016).
- [2] Y. Gao, C. S. S. Sandeep, J. M. Schins, A. J. Houtepen, and L. D. A. Siebbeles, *Nature Communications* **4**, 2329 (2013).
- [3] K. Wei, X. Zheng, X. Cheng, C. Shen, and T. Jiang, *Advanced Optical Materials* **4**, 1993 (2016).
- [4] G. Soavi, S. Dal Conte, C. Manzoni, D. Viola, A. Narita, Y. Hu, X. Feng, U. Hohenester, E. Molinari, D. Prezzi, et al., *Nature Communications* **7**, 11010 (2016).
- [5] Y.-Z. Ma, L. Valkunas, S. L. Dexheimer, S. M. Bachilo, and G. R. Fleming, *Phys. Rev. Lett.* **94**, 157402 (2005).
- [6] S. Wang, M. Khafizov, X. Tu, M. Zheng, and T. D. Krauss, *Nano Letters* **10**, 2381 (2010).
- [7] E. Engel, K. Leo, and M. Hoffmann, *Chemical Physics* **325**, 170 (2006).
- [8] T.-Q. Nguyen, I. B. Martini, J. Liu, and B. J. Schwartz, *The Journal of Physical Chemistry B* **104**, 237 (2000).
- [9] D. Sun, Y. Rao, G. A. Reider, G. Chen, Y. You, L. Brezin, A. R. Harutyunyan, and T. F. Heinz, *Nano Letters* **14**, 5625 (2014).
- [10] S. Mouri, Y. Miyauchi, M. Toh, W. Zhao, G. Eda, and K. Matsuda, *Phys. Rev. B* **90**, 155449 (2014).
- [11] N. Kumar, Q. Cui, F. Ceballos, D. He, Y. Wang, and H. Zhao, *Phys. Rev. B* **89**, 125427 (2014).
- [12] L. Yuan and L. Huang, *Nanoscale* **7**, 7402 (2015).
- [13] M. Amani, D.-H. Lien, D. Kiriya, J. Xiao, A. Azcatl, J. Noh, S. R. Madhvapathy, R. Addou, S. KC, M. Dubey, et al., *Science* **350**, 1065 (2015).
- [14] S. Wang, J. Wang, W. Zhao, F. Giustiniano, L. Chu, I. Verzhbitskiy, J. Zhou Yong, and G. Eda, *Nano Letters* **17**, 5156 (2017).
- [15] B. Han, C. Robert, E. Courtade, M. Manca, S. Shree, T. Amand, P. Renucci, T. Taniguchi, K. Watanabe, X. Marie, et al., *Phys. Rev. X* **8**, 031073 (2018).
- [16] M. Manca, M. M. Glazov, C. Robert, F. Cadiz, T. Taniguchi, K. Watanabe, E. Courtade, T. Amand, P. Renucci, X. Marie, et al., *Nature Communications* **8**, 14927 (2017).
- [17] J. Binder, J. Howarth, F. Withers, M. Molas, T. Taniguchi, K. Watanabe, C. Faugeras, A. Wysmolek, M. Danovich, V. Falko, et al., *Nature Communications* **10**, 1 (2019).
- [18] N. M. Gabor, J. C. Song, Q. Ma, N. L. Nair, T. Taychatanapat, K. Watanabe, T. Taniguchi, L. S. Levitov, and P. Jarillo-Herrero, *Science* **334**, 648 (2011).
- [19] J. C. Song, M. S. Rudner, C. M. Marcus, and L. S. Levitov, *Nano Letters* **11**, 4688 (2011).
- [20] D. Sun, G. Aivazian, A. M. Jones, J. S. Ross, W. Yao, D. Cobden, and X. Xu, *Nature Nanotechnology* **7**, 114 (2012).
- [21] Q. A. Vu, J. H. Lee, V. L. Nguyen, Y. S. Shin, S. C. Lim, K. Lee, J. Heo, S. Park, K. Kim, Y. H. Lee, et al., *Nano Letters* **17**, 453 (2017).
- [22] L. Britnell, R. Gorbachev, R. Jalil, B. Belle, F. Schedin, A. Mishchenko, T. Georgiou, M. Katsnelson, L. Eaves, S. Morozov, et al., *Science* **335**, 947 (2012).
- [23] Q. Ma, T. I. Andersen, N. L. Nair, N. M. Gabor, M. Masicotte, C. H. Lui, A. F. Young, W. Fang, K. Watanabe, T. Taniguchi, et al., *Nature Physics* **12**, 455 (2016).
- [24] M. S. Choi, G.-H. Lee, Y.-J. Yu, D.-Y. Lee, S. H. Lee, P. Kim, J. Hone, and W. J. Yoo, *Nature Communications* **4**, 1624 (2013).
- [25] H. Jeong, H. M. Oh, S. Bang, H. J. Jeong, S.-J. An, G. H. Han, H. Kim, S. J. Yun, K. K. Kim, J. C. Park, et al., *Nano Letters* **16**, 1858 (2016).
- [26] M. M. Furchi, D. K. Polyushkin, A. Pospischil, and T. Mueller, *Nano Letters* **14**, 6165 (2014).
- [27] G. Moody, J. Schaibley, and X. Xu, *J. Opt. Soc. Am. B* **33**, C39 (2016).
- [28] H. Wang, C. Zhang, and F. Rana, *Nano Letters* **15**, 339 (2015).
- [29] Y. Yu, Y. Yu, C. Xu, A. Barrette, K. Gundogdu, and L. Cao, *Phys. Rev. B* **93**, 201111(R) (2016).
- [30] D.-H. Lien, S. Z. Uddin, M. Yeh, M. Amani, H. Kim, J. W. Ager, E. Yablonovitch, and A. Javey, *Science* **364**, 468 (2019).
- [31] K. C. Santosh, R. C. Longo, R. Addou, R. M. Wallace, and K. Cho, *Nanotechnology* **25**, 375703 (2014).
- [32] L. Rota, P. Lugli, T. Elsaesser, and J. Shah, *Phys. Rev. B* **47**, 4226 (1993).
- [33] A. Grubisic Cabo, J. A. Miwa, S. S. Grønberg, J. M. Riley, J. C. Johannsen, C. Cacho, O. Alexander, R. T. Chapman, E. Springate, M. Grioni, et al., *Nano Letters* **15**, 5883 (2015).
- [34] Z. Nie, R. Long, L. Sun, C.-C. Huang, J. Zhang, Q. Xiong, D. W. Hewak, Z. Shen, O. V. Prezhdo, and Z.-H. Loh, *ACS Nano* **8**, 10931 (2014).
- [35] T. B. Arp, D. Pleskot, V. Aji, and N. M. Gabor, *Nature Photonics* **13**, 245 (2019).
- [36] C. J. Ciccarino, T. Christensen, R. Sundaraman, and P. Narang, *Nano Letters* **18**, 5709 (2018).
- [37] R. M. Martin and R. M. Martin, *Electronic structure: basic theory and practical methods* (Cambridge University Press, 2004).